Biomaterials 311 (2024) 122686

Contents lists available at ScienceDirect

Biomaterials

journal homepage: www.elsevier.com/locate/biomaterials

Engineering microvascular networks using a *KLF2* reporter to probe flow-dependent endothelial cell function

Adriana Blazeski [a,b,c], Marie A. Floryan [c], Yuzhi Zhang [a], Oscar R. Fajardo Ramírez [a], Elamaran Meibalan [a], Jesús Ortiz-Urbina [a], Emmanouil Angelidakis [d], Sarah E. Shelton [d,e], Roger D. Kamm [c,d], Guillermo García-Cardeña [a,b,*]

[a] Center for Excellence in Vascular Biology, Department of Pathology, Brigham and Women's Hospital, USA and Harvard Medical School, Boston, MA, USA
[b] Cardiovascular Disease Initiative, Broad Institute of MIT and Harvard, Cambridge, MA, USA
[c] Department of Mechanical Engineering, Massachusetts Institute of Technology, Cambridge, MA, USA
[d] Department of Biological Engineering, Massachusetts Institute of Technology, Cambridge, MA, USA
[e] Department of Medical Oncology, Dana Farber Cancer Institute, Boston, MA, USA

ARTICLE INFO

Keywords:
Engineered microvascular networks
Shear stress
Flow reporter
Microfluidic chip
Flow sensors

ABSTRACT

Shear stress generated by the flow of blood in the vasculature is a potent regulator of endothelial cell function and vascular structure. While vascular responses to flow are complex and context-dependent, endothelial cell signaling in response to shear stress induced by laminar flows is coordinated by the transcription factor *KLF2*. The flow-dependent expression of *KLF2* in endothelial cells is associated with a quiescent, anti-inflammatory phenotype and has been well characterized in two-dimensional systems but has not been studied in three-dimensional *in vitro* systems. Here we develop engineered microvascular networks (MVNs) that incorporate a *KLF2*-based endothelial cell flow sensor within a microfluidic chip, apply continuous flow using an attached microfluidic pump, and study the effects of this flow on vascular structure and function. We found that application of flow to MVNs for 48 h resulted in increased expression of the *KLF2* reporter, larger vessel diameters, and decreased vascular branching and resistance. Notably, vessel diameters after the application of flow were independent of initial MVN morphologies. Finally, we found that MVNs exposed to flow have improved vascular barrier function and decreased platelet adhesion. MVNs with *KLF2*-based flow sensors represent a novel, powerful tool for evaluating the structural and functional effects of flow on engineered three-dimensional vascular systems.

1. Introduction

Models of human microvascular physiology have been instrumental in bridging the gap between two-dimensional *in vitro* systems and animal models for studies of vascular biology and mechanisms of disease. In particular, self-assembled microvascular networks (MVNs) can recapitulate tissue-specific heterocellular interactions, complex three-dimensional geometries, and cell-matrix signaling [1] to mimic the structure and function of *in vivo* vascular beds. These systems have been used to model a number of aspects of vascular biology, including vasculogenesis [2–4], effects of interstitial flow on vascular network formation [5], and transport of biologics across the vascular barrier [6]. Additionally, MVNs with tissue-specific cells have been used to model biological environments like the blood-brain barrier [7] and metastasizing tumors [8].

A key element that can further improve engineered MVNs as physiological representations of human vasculature is the incorporation of flow. *In vivo*, vessels are constantly exposed to hemodynamic forces generated by the flow of blood, which regulates a host of processes during vascular development and homeostasis [9,10]. In particular, mean shear stress, the frictional force per unit area tangential to the endothelial surface, varies across vessels in the body from 1 dyn/cm^2 to 50 dyn/cm^2 (0.1 Pa–5 Pa) [11], and has been shown to regulate vascular remodeling, homeostasis, and cell fate specification [12]. Importantly, these processes are highly dependent on the direction, pulsatility, and magnitude of shear stress in the vasculature [13]. Additionally, it has

* Corresponding author. Center for Excellence in Vascular Biology, Department of Pathology, Brigham and Women's Hospital, USA and Harvard Medical School, Boston, MA, USA.
E-mail address: guillermo_garcia-cardena@hms.harvard.edu (G. García-Cardeña).

https://doi.org/10.1016/j.biomaterials.2024.122686
Received 1 February 2024; Received in revised form 12 June 2024; Accepted 23 June 2024
Available online 25 June 2024

been proposed that endothelial cells (EC) are tuned to a range of shear stresses that promote homeostasis, acquire an inflammatory phenotype in response to shear stress outside of this range, and will remodel vascular diameter in order to return to this setpoint [14].

Because of this, readouts of vascular physiology in response to flow are needed to indicate the presence of threshold levels of shear stress and a corresponding effect on EC phenotype. In this context, expression of Krüppel-like factor 2 (*KLF2*), a transcription factor that has been identified as a key integrator of endothelial response to shear stress [15–18], is ideally suited as a cell-based readout of flow. The expression of *KLF2* is induced in EC by laminar flow [19] and has been shown to regulate pathways involved in vessel development, inflammation, thrombosis, and vascular tone [15]. Its expression is associated with a quiescent, vasoprotective endothelial phenotype that has been extensively characterized [15,17,20]. Importantly, a cellular *KLF2* reporter system has been developed, which recapitulates key aspects of the expression of the endogenous gene [21].

In this study, we incorporate a *KLF2*-based EC flow sensor into MVNs within a microfluidic system and apply circulating, continuous, unidirectional flow. We show that shear stress activates the *KLF2* reporter in EC within a complex, three-dimensional network of vessels and that these networks respond by altering their geometry, including increasing vascular diameter. Additionally, we documented that flow conditioning improves the barrier function of MVNs and reduces platelet adhesion in the vessels. We further show that vessels with different starting geometry remodel to a similar geometric endpoint in response to flow. This system represents an engineering approach to perfused microvascular models that incorporates a built-in cellular flow reporter system. Importantly, it provides a unique readout for the levels of shear stress magnitude and timing of exposure necessary to elicit a *KLF2*-associated endothelial phenotype, which can now be incorporated into engineered models of human microvascular physiology.

2. Materials and methods

Cell culture and evaluation of monolayers. Human Umbilical Vein Endothelial cells (HUVEC) were selected for use in this study based on their ability to reliably form microvascular networks [3,5,6] and the well-understood connection between shear stress and *KLF2* expression in HUVEC cultures in 2D [15,16,22]. HUVECs were isolated and cultured [9] and subsequently transduced with a pTRH-mCMV-dscGFP lentiviral reporter construct and sorted using fluorescence-activated cell sorting (FACS) to obtain cells with low GFP expression at baseline that will activate GFP in response to flow, as previously described [21]. One pool of HUVEC, derived from one set of donors, was used throughout the studies. *KLF2*-GFP HUVEC were maintained in VascuLife VEGF medium (Lifeline Cell Technology) prepared using the supplements as directed by the manufacturer, with the exception of heparin sulfate, which was added at a lower concentration (0.19 U/mL final concentration). *KLF2*-GFP HUVEC were grown to 90 % confluency prior to use in MVNs and used at passage 14. Human lung fibroblasts (Lonza) at passage 7 were maintained in FibroLife S2 Fibroblast Medium (Lifeline Cell Technology) and cultured until 50–70 % confluency prior to use in MVNs. For some studies, fibroblasts were fluorescently labelled by lentiviral transduction with rLV.EF1.mCherry-9 (Takara Bio USA). All cells were maintained at 37 °C and 5 % CO_2 throughout culture.

HUVEC monolayers were exposed to flow using a cone and plate device programmed to generate laminar flow and a specified shear stress (5 dyn/cm^2 and 10 dyn/cm^2, equivalent to 0.5 Pa and 1 Pa, respectively, in this study) and assayed for *KLF2*-GFP expression. As previously described [21], *KLF2*-GFP HUVEC were plated on plastic substrates (QC Precision Machining) coated with 0.1 % gelatin (Becton Dickinson) at a density of 6×10^4 cells/cm^2 24 h prior to the start of flow. One hour prior to flow initiation, the medium was replaced with new medium supplemented with 1.7 % dextran (Catalog No. D5376, Millipore Sigma). Monolayers were maintained under flow for 24 h at 37 °C, 5 % CO_2 in a custom dynamic flow system [22]. Immediately after the cessation of flow, monolayers were imaged for GFP expression using an Axiovert microscope (Zeiss), and subsequently dissociated, stained with for VE-cadherin, and analyzed using FACS, as described below.

Fabrication of microfluidic device and pump. Device and pump designs were created in Fusion 360 (Autodesk) and component molds were milled using a Computer Numerical Control (CNC) Milling Machine (Bantam Tools). The gel channel in the microfluidic device measured 3.0 mm in width and 8.3 mm in length. Polydimethylsiloxane (PDMS, Dow Corning Sylgard 184, Ellsworth Adhesives) was mixed at a ratio of 10:1, degassed for 30 min, poured into milled molds, degassed a second time for 30 min, and cured in an oven at 65 °C overnight. Microfluidic devices were subsequently fabricated as previously described [23,24]: individual PDMS devices were cut, gel and media ports were punched out using biopsy punches (Integra Miltex), and devices were sterilized by autoclave for 25 min. Devices and clean glass coverslips (VWR) were plasma treated (Expanded plasma cleaner, Harrick Plasma), bonded, and placed in an oven at 75 °C overnight. Pump PDMS layers and membranes were trimmed, ports were punched out, and individual pumps were assembled after plasma bonding, as previously described [25].

Formation of microvascular networks. *KLF2*-GFP HUVEC and fibroblasts were suspended in a fibrin gel and seeded as previously described [6]. HUVEC and fibroblasts were dissociated from cell culture flasks using TrypLE Express (Thermo Fisher Scientific), suspended in a solution of VascuLife and 6 mg/mL fibrinogen from bovine plasma (Millipore Sigma) at a concentration of 14 million/mL and 2 million/mL HUVEC and fibroblasts, respectively. For each device, 7 μL of the cells and fibrinogen solution was combined with 7 μL of VascuLife with 2.8 U/mL thrombin from bovine plasma (Millipore Sigma) prior to injection in the device gel port (for a final concentration of 7 million/mL HUVEC, 1 million/mL fibroblasts, 1.4 U/mL of thrombin, and 3 mg/mL of fibrinogen). For some experiments, the thrombin concentration was decreased to 1.1 U/mL in order to slow gelling time, resulting in vessels with larger diameters, as indicated in the text. The remaining HUVEC were replated for seeding monolayers. Devices were incubated at 37 °C for 10 min prior to adding VascuLife medium in the media channels. Devices became lumenized and perfusable on day 4–5 of culture. Media was changed daily through the media channels on either side of the gel containing MVNs.

HUVEC monolayers were seeded along the sides of the gel channels of each device on day 4 of culture [6]. After removing the media, 30 μg/mL fibronectin (Millipore Sigma) was introduced into each media channel and the devices were incubated for 30 min prior to HUVEC seeding. In each device, the fibronectin was removed from one media channel and a suspension of 0.5–1 million/mL HUVEC was added to the channel. The device was tilted so that the cell suspension would settle on top of the central gel channel and left for 10 min before repeating the procedure in the other media channel. Each device was then incubated for 10 min at 37 °C prior to replacing the media in both channels.

Application of flow in MVNs and measurement of flow speeds. The hydraulic resistance of the MVNs was measured by attaching 1 mL syringe barrels to each media port of the devices, adding media to establish an initial pressure difference of approximately 245 Pa across the MVNs, and monitoring the changes in the pressure head difference at 15-min intervals over 75 min. The media height difference between the two sides of the device over time could be fitted using the formula:

$$\frac{\Delta z(t)}{\Delta z(0)} = e^{-\frac{2\rho g}{A_r R_N} t}$$

where Δz is the difference in media height, t is time, ρ is the density of cell culture media (~993 kg/m^3), g is the standard gravity (9.8 m/s^2), A_r is the cross-sectional area of the syringe reservoirs, and R_N is the bulk hydraulic resistance of the MVNs. R_N could then be calculated from:

$$R_N = -\frac{2\rho g}{A_r m}$$

where m is the slope of the line fitted to the natural logarithm of the height difference.

The hydraulic MVN resistance was used in a combined lumped-element and finite-element model [25] to predict the vascular wall shear stresses resulting from a range of pressures applied to the pump chamber. For flow experiments, pump pressures were selected based on these modeling results in order to achieve physiological vascular wall shear stress (5 dyn/cm^2 to 15 dyn/cm^2, or 0.5 Pa–1.5 Pa). Each microfluidic device was attached to a pump and media was circulated through the microfluidic devices by applying cyclical air pressure through a solenoid and into the pumping chamber, as detailed previously [25]. Flow was applied on day 5–8 of culture, when MVNs were fully formed and perfusable. Unless otherwise specified, flow was applied to MVNs for 48 h prior to MVN evaluation.

To determine the flow speeds within vessels, MVNs were stained with 1:200 DyLight 594 UEA I lectin (Vector Laboratories) in VascuLife medium for 20 min at 37 °C before 1 μm fluorescent beads (Millipore Sigma) were added to the cell culture media in the microfluidic devices and pumps. Vessels and beads were visualized on an Axiovert microscope (Zeiss) and 60 fps video recordings of bead flows in response to application of 3–9 kPa of pressure at the pumping chambers were acquired. Pumps were run for 5 min at each pressure to reach stable flow speeds before acquisition of 60 s videos. Custom MATLAB (MathWorks) scripts were used analyze bead speeds. First, videos were first divided into 60 frame (for 3 kPa and 6 kPa flows) or 30 frame (for 9 kPa flows) segments. For each of these segments, maximum signal intensity projections over time were generated and the first frame was subtracted, leaving the bead tracks. These images were then thresholded to segment out the bead tracks, the connected components were determined, and the time at each point along each connected component was computed. The tracks were skeletonized and their length was calculated. Finally, the speed of each track was computed from the length and the start and end times of each component. Average bead speeds were determined by computing the mean of all of the bead tracks across all samples for each pump pressure.

Imaging of MVNs and measurement of vascular permeability. Permeability of MVNs was measured by introducing fluorescent dextran (Texas Red, 70 kDa MW, Thermo Fisher Scientific) into the media channels of each microfluidic device and quantifying the change in intravascular and extravascular fluorescence levels at the centers of the MVNs after 12 min, as previously described [6]. MVNs were imaged using an Olympus FV1000 confocal microscope at 37 °C and using a 10x objective. Confocal z-stack images were acquired at a resolution of 0.5 pixels/μm at a z-spacing of 5 μm every 12 min. Image segmentation and average fluorescent intensity measurements were conducted using ImageJ and vascular permeability calculations were subsequently performed as detailed previously [6].

Confocal z-stack images of *KLF2*-GFP signal were acquired as described for permeability above. Fiji was used to create maximum intensity projection images, apply Otsu thresholding to segment out GFP-positive signal, and measure the area and signal intensities of GFP-positive regions. GFP-positive areas are represented as a percentage of the total area of each image and GFP intensities are normalized to the lowest average intensity in a static sample of the same batch of MVNs.

To perform time course *KLF2*-GFP imaging, MVNs were stained with UEA I lectin as detailed above prior to the start of flow. Samples were maintained at 37 °C, 5 % CO_2 in a custom enclosure while confocal z-stack images were acquired every 20 min as detailed above. GFP-positive area was determined using Fiji as detailed above, normalized from 0 to 1 using the following

$$Normalized\ GFP^{+}Area\ (t) = \frac{GFP^{+}Area\ (t) - GFP^{+}Area\ (t=0)}{Maximum\ GFP^{+}Area\ - GFP^{+}Area\ (t=0)}$$

where t is time. Traces were fitted using an exponential curve to determine the time constant.

Immunofluorescent staining and imaging. MVNs were fixed in 4 % paraformaldehyde solution (Thermo Fisher Scientific) for 15 min, and rinsed three times with Phosphate-Buffered Saline (PBS, Thermo Fisher Scientific) for 5 min each time. All solutions were applied through the media channels of the microfluidic devices, placing the devices on a rocker during fixation and staining. Blocking and permeabilization was performed by applying a solution of 10 % goat serum (Gibco) and 1 % Triton X-100 (Fisher Scientific) in PBS for 3 h at room temperature. The following primary antibodies were applied in 1 % goat serum (Gibco) and 0.2 % Triton X-100 in PBS overnight at 4 °C: primary mouse antibody against human CD144/VE-cadherin (BD Pharminogen, 1:50 dilution), primary mouse antibody against human VCAM-1 (Clone E1/6, a gift from Michael A. Gimbrone Lab, 1:20 dilution), primary mouse antibody against E-selectin/P-selectin (CD62 E/P, R&D Systems, 10 μg/mL), and primary rabbit antibody against cleaved Caspase-3 (Asp175, #9661, Cell Signaling Technology, 1:400 dilution). Samples were subsequently rinsed for 6 h using frequent changes of PBS solution. Samples were incubated in a 1:200 dilution of goat anti-mouse IgG1 Alexa Fluor 647 (Thermo Fisher Scientific), goat anti rabbit IgG Alexa Fluor 568 (Thermo Fisher Scientific) and 300 nM DAPI (Thermo Fisher Scientific) overnight at 4 °C. MVNs were rinsed by frequent exchanges in PBS for several hours, and left in PBS overnight at 4 °C before imaging as described above for vascular permeability, with a z-spacing of 2 μm.

Calculation of flow rates and wall shear stresses. Confocal images of static MVNs perfused with dextran were acquired as described above and tiled to span the entire width of the vasculature between the media channels. We used the micro-Vasculature Evaluation System algorithm to perform 3D vessel segmentation, skeletonization, and calculation of flow rates, speeds, and wall shear stresses in each branch [26]. For each MVN, boundary conditions were set such that the pressure across the network resulted in an average vessel flow speed corresponding to the average bead speed measured in that particular MVN.

Analysis of gene expression: For gene expression in sorted cells, cells were first extracted from MVNs by manually cutting out the gel from the microfluidic devices and digesting each gel in 500 μL of 0.5 mg/mL Liberase TM (Millipore Sigma) in DMEM (Thermo Fisher Scientific) for 30 min on ice with intermittent agitation [24]. Cells from 5 devices were pooled, filtered to remove debris, stained with Alexa Fluor 647 Mouse Anti-Human CD144 antibody (Catalog No. 561567, BD Pharminogen) and sorted using fluorescence activated cell sorting (FACS) to isolate ECs for subsequent gene expression analysis. RNA was isolated by lysing cells using buffer RLT (Qiagen) and purified using RNeasy Micro Kit (Qiagen). Reverse transcription was performed using High-Capacity RNA-to-cDNA Kit (Thermo Fisher Scientific). Quantitative real-time polymerase chain reaction (qRT-PCR) was performed using Taqman PCR Master Mix (Applied Biosystems) and samples were amplified on an ABI Prism 7900HT Fast Detection System (Applied Biosystems). Gene expression was normalized against GAPDH endogenous controls.

To perform gene expression analysis on unsorted cells, buffer RLT (Qiagen) was perfused directly through MVNs for 1 h. Reverse transcription was performed as described above. PCR was performed as detailed above using the QuantStudio 6 Pro Real-Time PCR System (Thermo Fisher Scientific). Expression of *CDH5* was normalized to *GAPDH*, while all other genes were normalized to *CDH5* to assess the relative expression of transcripts in endothelial cells.

Analysis of vessel geometry. Total vascular area was calculated from maximum intensity projection images of MVNs perfused with dextran. Images were processed using AutoTube software [27], with the following settings: pre-processing by adaptive histogram equalization, illumination correction, and image denoising through Block-Matching and 3D Filtering, tube detection with the Multi-Otsu thresholding, and tube analysis with removal of short ramification that are less than 20

pixels of length and merging of branch points within a radius of 22 pixels. Number of branches, branch length, and diameter were calculated by analyzing confocal z-stacks of MVNs perfused with dextran with the micro-Vasculature Evaluation System algorithm, which performs vessel segmentation, skeletonization, branch point analysis, and calculation of vascular morphological parameters in 3D [26]. To visualize vascular diameters, MVN surfaces were constructed from dextran images using Imaris software (Oxford Instruments) and clipped along the xz plane to reveal vessel openings.

Perfusion of platelets in MVNs. Human whole blood collected in sodium citrate (Research Blood Components, LLC) was centrifuged for 15 min at 120 g to separate the plasma and buffy coat layers from the red blood cells. Suspended platelets were labelled by incubating in 0.5 μg/mL CD41 antibody (Catalog No. 303725, Biolegend) for 20 min at room temperature. Afterwards, the platelet solution was diluted 1:4 in human plasma like medium (Thermo Fisher Scientific, A4899101), containing 45.701 mg/ml magnesium chloride and 42.13 mg/ml magnesium sulfate, and recalcified by addition of 10 mM $CaCl_2$ immediately prior to perfusion through MVNs. To add platelets to the MVNs, media from one channel was removed, the channel was filled with platelet solution, media from the other channel was removed, and a platelet solution of equal volume to the solution in the other channel was added, similar to previously-described methods [28]. For MVNs cultured under flow (48 h of flow with a pump inlet pressure of 6 kPa, as described in the manuscript), the pumps were stopped and removed prior to addition of the platelets in the system. Unbound platelets were washed out of MVNs by sequential media changes prior to imaging samples to determine platelet retention. MVNs and platelets were imaged on a confocal microscope, just as described for permeability measurements. The percentage of $CD41^+$ area in each image was determined from maximum intensity projections, using the same method described for determining the percentage area expressing *KLF2*-GFP described above.

Statistics. Average values are reported as mean ± standard deviation and samples sizes are reported in figure legends. Statistical analysis was performed using GraphPad Prism software. Parametric, two-tailed t tests were applied to analyses involving two groups and ordinary one way ANOVA with Tukey's multiple comparison tests were applied to analyses involving more than two groups. * indicates $p < 0.05$, ** indicates $p < 0.01$, *** indicates $p < 0.001$, **** indicates $p < 0.0001$, and ns indicates $p > 0.05$.

3. Results

Microfluidic system with engineered vasculature containing flow-responsive endothelial cell reporter and *on chip* pump. Our microfluidic platform includes a chip with a central channel that houses engineered MVNs bordered by media channels that are connected directly to a pump [25] (Fig. 1a and b). This *on chip* pump is composed of two layers of PDMS with a silicone membrane between them that can be actuated at the pumping chamber to displace fluid and move cell culture media through the system. Two fluid capacitors are used to establish a pressure difference that drives flow across the microfluidic device, while two check-valves are incorporated to ensure low-pulsatility, unidirectional flow (Fig. 1b). The pump is operated by applying cyclical, positive air pressure at the pumping chamber under the control of a solenoid at a frequency of 1 Hz. The pump inlet and outlet ports interface with the media channels bordering the MVNs. MVNs are formed by encapsulating human umbilical vein endothelial cells (HUVEC) and human lung fibroblasts into a fibrin gel and allowing them to self-assemble into lumenized vessels over the course of 4–5 days [23,29]. EC incorporated a reporter based on GFP expression driven by a 1.1 Kb segment of the proximal human *KLF2* promoter [21], allowing them to act as flow sensors in the system (Fig. 1a). At 5 days of culture, MVNs are fully perfusable with dextran (Fig. 1c), indicating that they have formed a connected bed of patent vessels through which media circulates. As previously documented, EC containing the *KLF2* reporter and cultured as confluent monolayers responded to application of laminar flow by turning on GFP fluorescence (Supplementary Fig. 1). In three-dimensional MVNs, GFP expression appeared in EC cultured under flow ("flow MVNs") but not in MVNs cultured under static conditions ("static MVNs") (Fig. 1d). Static and flow MVNs were subsequently dissociated into single cells and stained for VE-cadherin before being separated into EC ($VE\text{-}cadherin^+$) and fibroblast ($VE\text{-}cadherin^-$) populations using flow cytometry (Fig. 1e, Supplementary Fig. 2). While fibroblasts dissociated from both static and flow MVNs had background levels of fluorescence, EC from flow MVNs exhibited an increase in GFP expression compared to those from static MVNs (Fig. 1f). Quantification of GFP expression in sorted EC indicated an increase in GFP-positive cells from 12.0 % in static MVNs to 56.2 % in flow MVNs (Fig. 1g). Additionally, EC from flow MVNs exhibited increased *KLF2* endogenous gene expression compared to ECs from static MVNs (Fig. 1h, n = 5 pooled devices). Further analysis of gene transcripts in static MVNs and MVNs after 48 h of flow performed in non-sorted samples indicated increased expression of *GFP* and endothelial nitric oxide synthase (*NOS3*) in flow MVNs, and decreased expression of angiopoietin-2 (*ANGPT2*) in flow MVNs (Fig. 1i). Altogether, our data indicate that this new system is suitable for creating three-dimensional MVNs with an EC-specific flow reporter serving as a descriptor of perfusion of the network and that application of flow in this system drives expression of flow-regulated genes.

Characterization of flow levels and timing in engineered system. Having determined that the *KLF2*-GFP reporter system can act as a flow sensor in MVNs, we next sought to determine the levels of flow needed to activate the GFP signal. To this end, we introduced fluorescent beads into our MVN and pump system and captured videos of their trajectories in the vessels (Supplementary Movie 1) in response to increasing pumping flow rates, achieved by increasing maximum air pressures applied at the pumping chambers. Bead positions were superimposed over time to generate trajectories (Fig. 2a), which were subsequently used to calculate average bead speeds within MVNs (Fig. 2b). Pressures of 3 kPa ("Low"), 6 kPa ("Medium"), and 9 kPa ("High") applied at the pumping chamber resulted in bead speeds of 0.8–1.0 mm/s, 1.7–2.1 mm/s, and 1.9–2.2 mm/s, 95 % confidence intervals of the means respectively, (Fig. 2b, n = 14–45 trajectories in n = 3 MVNs). The three levels of flow applied in our system all elicited *KLF2*-GFP expression in the MVNs (Fig. 2c). The percentage of imaging area positive for *KLF2*-GFP signal was significantly increased in all flow groups relative to static controls (7.3 ± 0.6 %, 10.6 ± 1.8 %, 14.2 ± 2.7 %, and 12.6 ± 2.9 % for static, low, medium, and high flow, respectively, where n = 3–11 per group), but did not differ significantly between flow groups (Fig. 2d). Normalized GFP intensity, indicative of the level of *KLF2* reporter expression in MVNs, was elevated significantly only in the medium and high flow groups compared to static controls (measuring 1.1 ± 0.1 for static, 1.3 ± 0.2 for low, 1.7 ± 0.2 for medium and 1.5 ± 0.4 high flow, respectively, where n = 3–11 per group), but did not differ significantly between these two flow groups (Fig. 2e). Additionally, we applied low pressures at the pumping chamber to determine the minimum flow speed that could activate the *KLF2*-GFP reporter. Pressures of 0.5 kPa and 1 kPa resulted in minimal and often pulsatile bead movements, with bead speeds of around 0.3 mm/s that did not significantly increase percentage of GFP-positive area or normalized GFP intensity beyond those of static controls (Supplementary Fig. 3). A pressure of 2 kPa at the pumping chamber resulted in bead speed of 0.5–0.6 mm/s, increased the percentage of GFP-positive area but not the normalized GFP intensity, and can be considered the minimum pump setting needed to elicit *KLF2*-GFP in MVNs. Based on all of these observations, we determined that 6 kPa of pressure applied at the pumping chamber, corresponding to "medium" flow, was sufficient to activate *KLF2*-GFP in our system and we used this level of flow for the remainder of the experiments in our study.

We next characterized the time course of *KLF2*-GFP activation in MVNs under flow by acquiring fluorescent confocal images across the volume of vessels over the course of nearly 10 h of flow

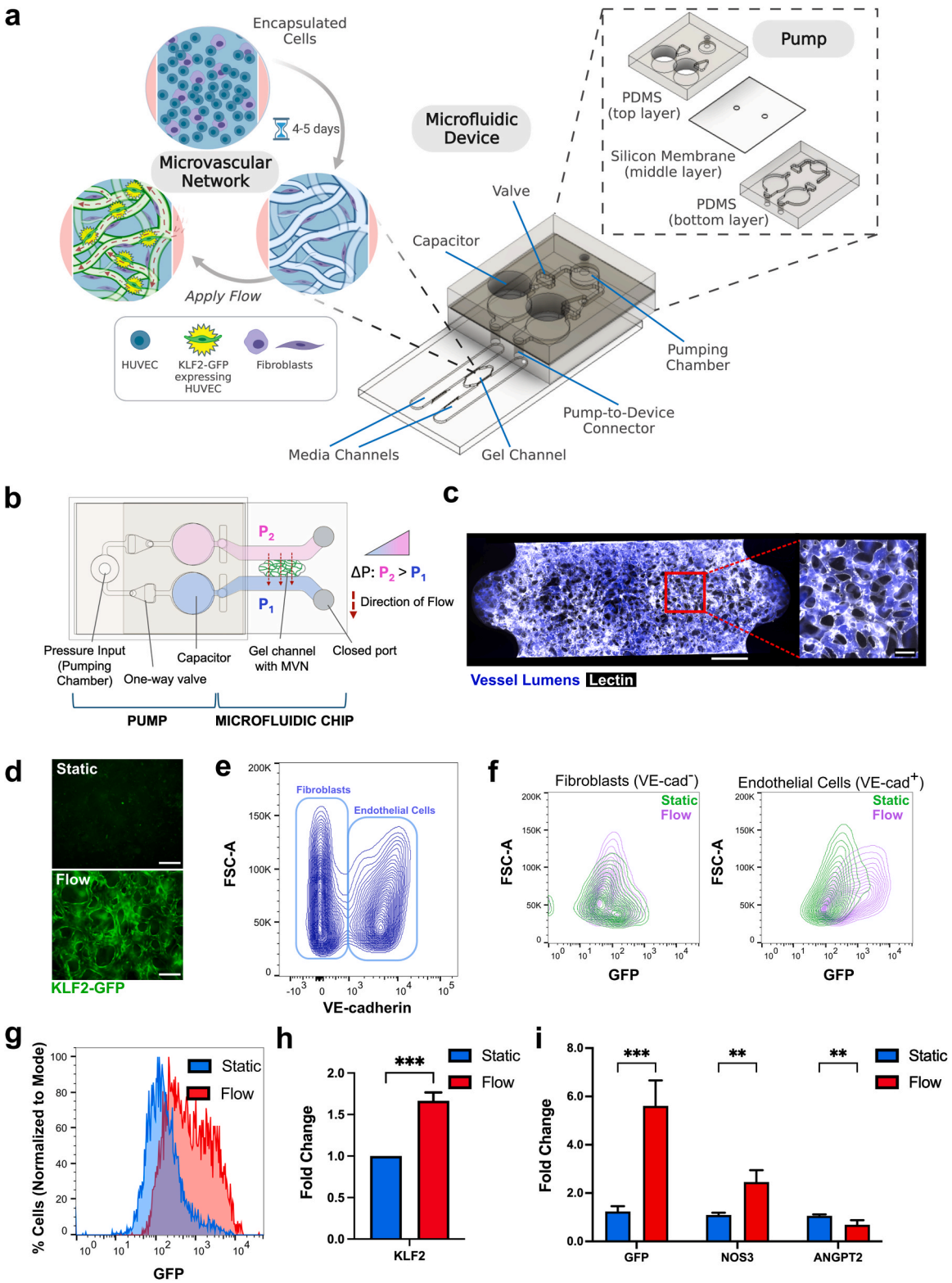

Fig. 1. Activation of *KLF2*-GFP reporter in MVNs with flow. a Schematic of microfluidic device and attached pump. HUVEC expressing *KLF2*-GFP and fibroblasts are seeded into the gel channel and self-assemble into MVNs. b Top view of pump and microfluidic chip illustrating the pressure difference that drives flow across the gel channel with the MVN. c Example of MVN stained with lectin (white) and perfused with fluorescent dextran (blue). Scale bar = 500 μm in full device image. Scale bar = 100 μm in close-up image of vasculature. d Image of *KLF*-GFP (green) expression in MVN after application of flow for 18 h and in MVN after culture in static conditions. Scale bars = 200 μm. e Flow cytometry analysis of cells in MVNs labelled with VE-cadherin. VE-cadherin$^+$ endothelial cells and VE-cadherin$^-$ fibroblasts are indicated by bounding rectangles. f Flow cytometry analysis of each population from MVNs cultured under static (green) and flow (purple) conditions. g Percentage of endothelial cells expressing GFP under static and flow conditions. h *KLF2* mRNA expression in endothelial cells extracted from MVNs and separated out using flow cytometry as in e (measurement from 5 pooled MVNs, with *GAPDH* as housekeeping gene). i Expression of flow regulated genes in MVNs kept without flow (static) and MVNs after 48 h of flow. Genes expression is normalized to *CDH5*. n = 4 MVN for each group. ** indicates $p < 0.01$ and *** indicates $p < 0.001$. (For interpretation of the references to colour in this figure legend, the reader is referred to the Web version of this article.)

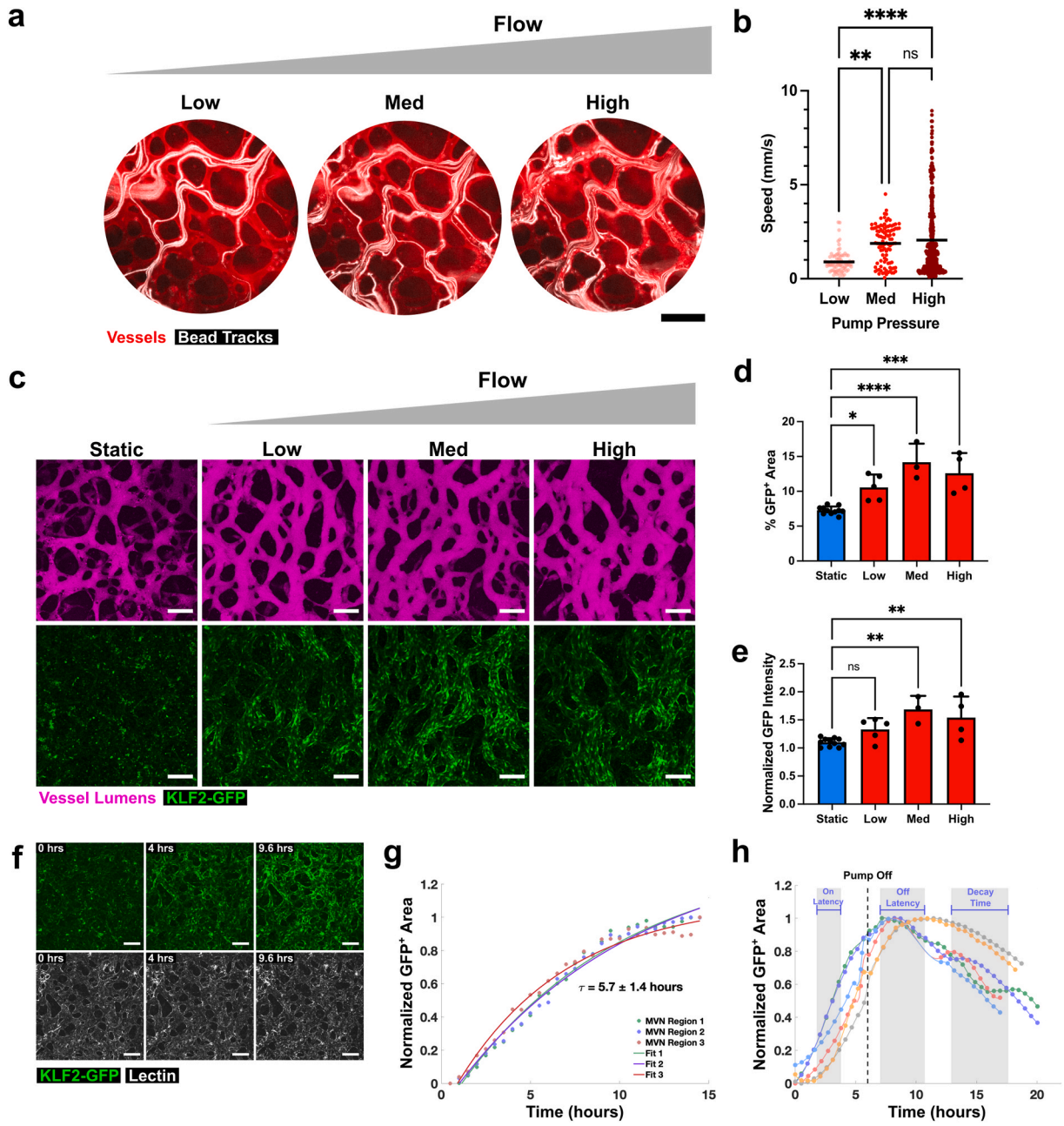

Fig. 2. Characterization of flow levels and time course in engineered MVN system. a Paths of fluorescent beads (white) in MVN (stained with red lectin) as pressure is increased in the pumping chamber. Scale bars = 200 μm. Each image represents a projection of bead location over 30 s. "Low", "Med", and "High", correspond to application of 3 kPa, 6 kPa, and 9 kPa pressure, respectively, in the pumping chamber. b Average bead speeds for range of pressures in the pumping chamber, calculated from images of bead speeds (n = 3 samples, with 14–45 bead paths per sample). c Examples of MVNs, visualized after perfusion with fluorescent dextran (magenta), and their *KLF2*-GFP expression (green) under static conditions or after 48 h of flow at the range of flow rates characterized in b. Scale bars = 200 μm. d Percent of total imaging area with *KLF2*-GFP signal. e *KLF2*-GFP signal intensity normalized to lowest intensity static sample. f Time series of z-stack confocal image projections of MVNs after the start of flow corresponding to medium pressure and acquired every 20 min. Samples were stained with lectin (white) to outline vessels. Scale bars = 200 μm. g Time course of *KLF2*-GFP expression in MVNs after initiation of flow. GFP-positive area for different regions in the MVN was modeled by an exponential fit and an average time constant for *KLF2*-GFP activation was calculated. τ is reported as mean ± standard deviation for 3 regions of interest. h Time course of *KLF2*-GFP expression in MVNs after turning on pump at 0 h and turning pump off at 6 h. Each trace represents an MVN and blue brackets denote mean ± standard deviation of "on latency" (time from pump start to 25 % of maximum signal), "off latency" (time from pump off to maximum signal), and "decay time" (time from pump off to 75 % of maximum signal), based on n = 6 MVNs. Data in b, d, and e reports mean and standard deviation from n = 3–11 MVNs. * indicates $p < 0.05$, ** indicates $p < 0.01$, *** indicates $p < 0.001$, **** indicates $p < 0.0001$, and ns indicates $p > 0.05$. (For interpretation of the references to colour in this figure legend, the reader is referred to the Web version of this article.)

(Fig. 2f–Supplementary Movie 2). Calculating the GFP-positive area from two-dimensional projections of these images and applying an exponential fit to the time course yielded a time constant for GFP expression of 5.7 ± 1.4 h (Fig. 2g, n = 3). The 48 h of flow applied in all subsequent experiments, therefore, were sufficient to ensure robust *KLF2*-GFP expression. Using the changes in GFP-positive area over time after initiation of flow, we determined that *KLF2*-GFP expression reached 25 % of its maximum at 1.8–3.8 h ("on latency"), persists for 1.0–4.7 h after the pump is turned off ("off latency") and reaches 75 % of its maximum value at 6.9–11.6 h after the pump is turned off ("decay

time", Fig. 2h, n = 6). By 24 h after cessation of flow, the *KLF2*-GFP in MVNs reaches pre-flow levels (Supplementary Fig. 4).

We used a computational approach [26] to determine the magnitudes of the wall shear stresses within the same set of MVNs at the beginning and at the end of 48 h of flow (Fig. 3). To accomplish this, we constructed a network of vascular branches based on confocal images spanning the width of individual MVNs (Fig. 3a) and applied a pressure difference across this network. For each MVN, we computed the pressure difference across the network that would result in an average flow speed for the vessels measured by pumping beads through the MVN using the "medium" flow pump setting. This allowed use to calculate the wall shear stress in each branch of the MVNs (Fig. 3b). The flow speeds in MVNs measured 4.9–5.1 mm/s and 5.1–5.4 mm/s (95 % confidence intervals of the means), prior to and after culture under flow, respectively (Fig. 3c, n = 7). The corresponding wall shear stresses varied across the branches within each MVN, but the average shear stress within MVNs was 7.1 ± 10.0 dyn/cm^2 (0.71 ± 1.0 Pa) and 6.1 ± 9.6 dyn/cm^2 (0.61 ±0 .96 Pa), before and after culture under flow, respectively (Fig. 3d, n = 4).

Changes in vascular morphology in response to flow. Because our system incorporates three-dimensional MVNs, it provided us with an opportunity to determine the effects of flow on vascular geometry. For these studies, we applied flow to MVNs for 48 h and compared them to control MVNs cultured under static (no flow) conditions. Fluorescent dextran perfused into MVNs was used to delineate the vascular lumens and to segment out vessels for morphologic analyses (Fig. 4a). Flow MVNs were characterized by strong *KLF2*-GFP expression along vascular walls (Fig. 4a) with corresponding increases in percent area positive for GFP (6.3 % ± 2.4 %, n = 8 static versus 12.3 % ± 3.4 %, n = 6 flow, Fig. 4b) and in normalized GFP intensity (1.1 ± 0.1, n = 8 static versus 1.7 ± 0.3, n = 7 flow, Fig. 4c) when compared to static MVNs. While the total area taken up by vessels, calculated from maximum intensity projections of images over the volume of dextran-perfused vessels, did not differ between static and flow MVNs (1.0 ± 0.1 mm^2, n = 12 for static and 1.1 ± 0.1 mm^2, n = 11 for flow, Fig. 4d), other aspects of branch geometry differed significantly between the two groups. Flow MVNs had a significantly lower number of branches (108 ± 14, n = 12 for static and 87 ± 12, n = 11 for flow, Fig. 4e), and a significantly greater average branch length (67.7 ± 8.1 μm, n = 12 for static and 77.3 ± 7.6 μm, n = 11 for flow, Fig. 4f) compared to static MVNs. Interestingly, cross-sectional views of flow MVNs revealed larger vessel lumens than those in static MVNs (Fig. 4g). Flow was associated with a significant increase in average vessel diameter (67.1 ± 12.5 μm, n = 12 for static and 96.8 ± 21.1 μm, n = 11 for flow, Fig. 4h) and a wider distribution of vessel diameters (Fig. 4i). EC in MVNs were elongated and oriented along vascular branches in both static and flow conditions (Fig. 4j). In both conditions, fibroblasts are evenly distributed throughout the gel surrounding MVNs (Supplementary Fig. 5).

Effect of vascular geometry on flow response. We next sought to determine whether the morphological remodeling of vessels under flow was affected by the initial geometry of the MVNs. The average vessel diameter in MVNs was varied by changing the concentration of thrombin that was mixed with fibrinogen prior to gel formation: 1.8 U/mL thrombin and 1.4 U/mL thrombin were used to make smaller and larger vessels, respectively. Decreasing thrombin concentration increased the gelling time, allowing the cells more time to settle in a smaller volume, and resulting in large vessels (Fig. 5a). This resulted in the generation of MVNs with an average diameter of 52.3 ± 1.7 μm (smaller vessels) or 59.8 ± 3.2 μm (larger vessels, Fig. 5e). Application of flow in both larger and smaller vessels increased the percent area

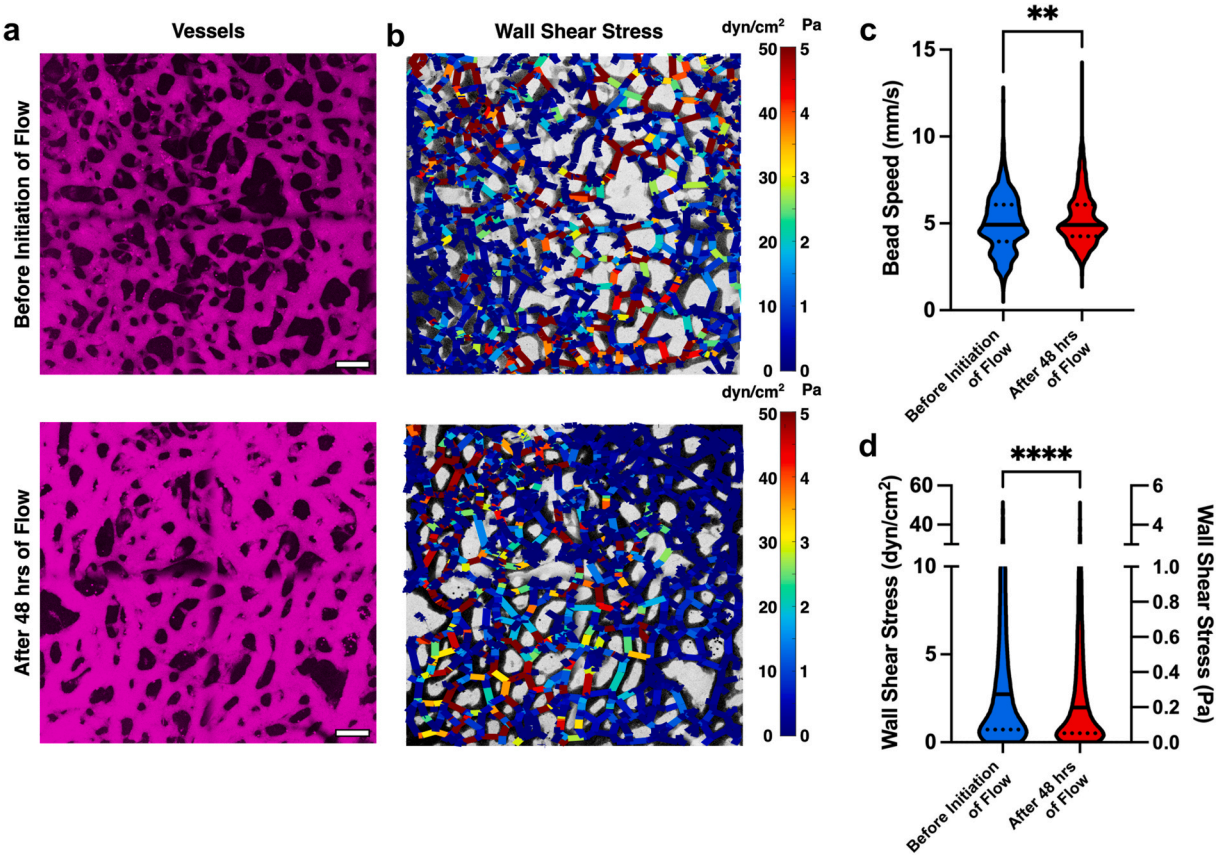

Fig. 3. Estimates of wall shear stress in MVNs. a Images of MVN before (top) and after (bottom) application of flow for 48 h. Scale bars = 200 μm and images span the width of the gel region. b Map of wall shear stress in each branch of MVN. c Speed of beads pumped through MVNs before and after culture under flow. n = 7 MVNs in c and n = 4 MVNs in d. Horizontal black lines indicate mean value for the group. ** indicates $p < 0.01$, and **** indicates $p < 0.0001$.

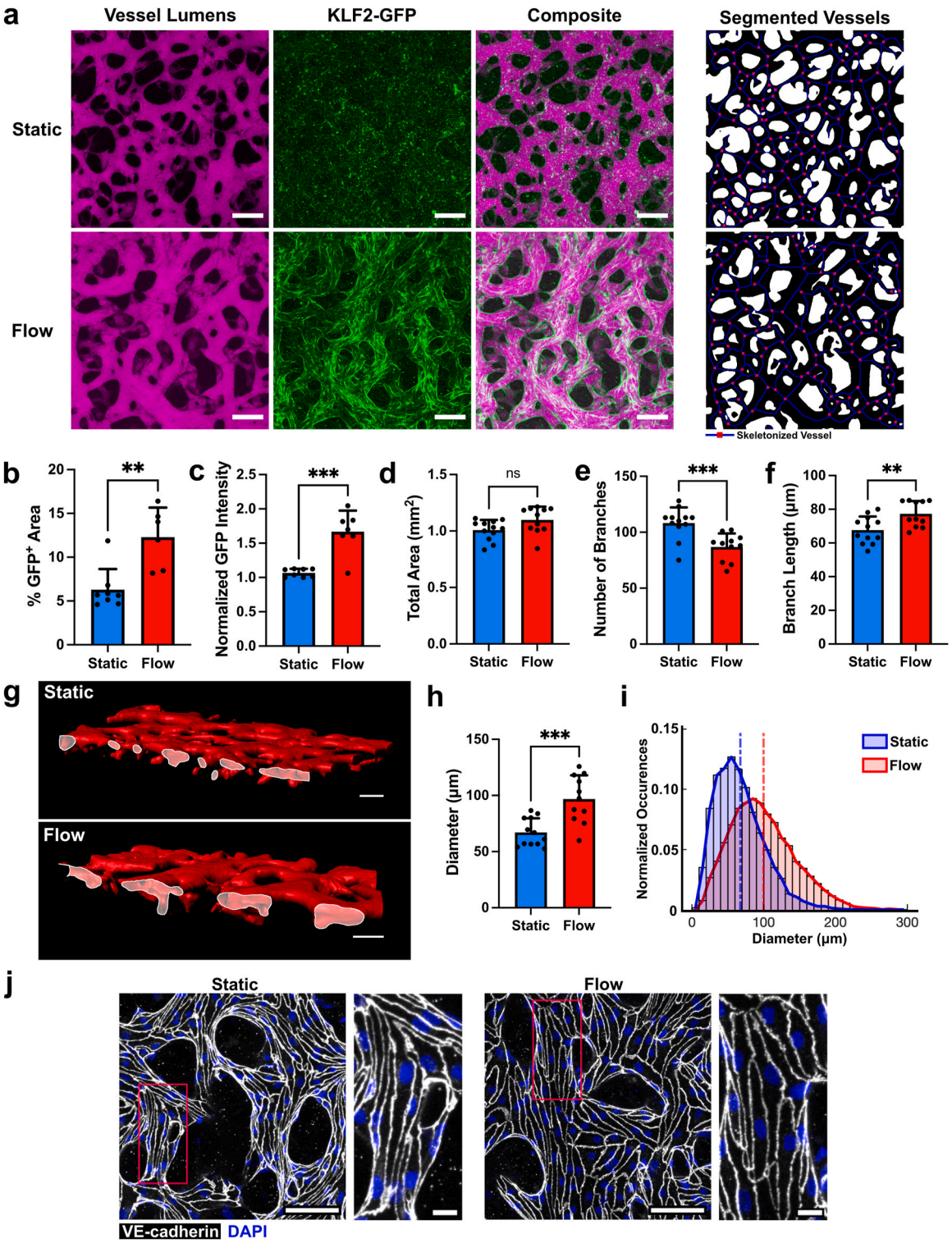

Fig. 4. Flow-induced changes in vascular geometry. a MVNs cultured under static (top) or flow (bottom) conditions. Vessels were perfused with fluorescent dextran (magenta) to visualize the intravascular space. MVNs cultured under flow expressed the *KLF2*-GFP reporter (green). Vessels were segmented out and skeletonized using these images (right). Scale bars = 200 μm b Percent of total imaging area with *KLF2*-GFP signal. c *KLF2*-GFP signal intensity normalized to lowest intensity static sample. d-f Number of branches, total area covered by vessels, and average branch length in MVNs. g Surface reconstruction of static MVNs (top) and MVNs under flow (bottom) cut across the xz plane to show vessel openings (outlined in white). h Average branch diameter in MVNs. i Distribution of vascular diameters in MVNs cultured under static (blue) and flow (red) conditions. Vertical dashed lines indicate average diameters across all samples in each group. In panels b–f and h, n = 11–12 MVNs per group. j VE-cadherin (white) in MVNs cultured under static and flow conditions. The full image area is shown on the left and the magnification of the region outlined in red is shown on the right. Scale bars = 100 μm in large area images and scale bars = 20 μm in magnified images. ** indicates $p < 0.01$, *** indicates $p < 0.001$, and ns indicates $p > 0.05$. (For interpretation of the references to colour in this figure legend, the reader is referred to the Web version of this article.)

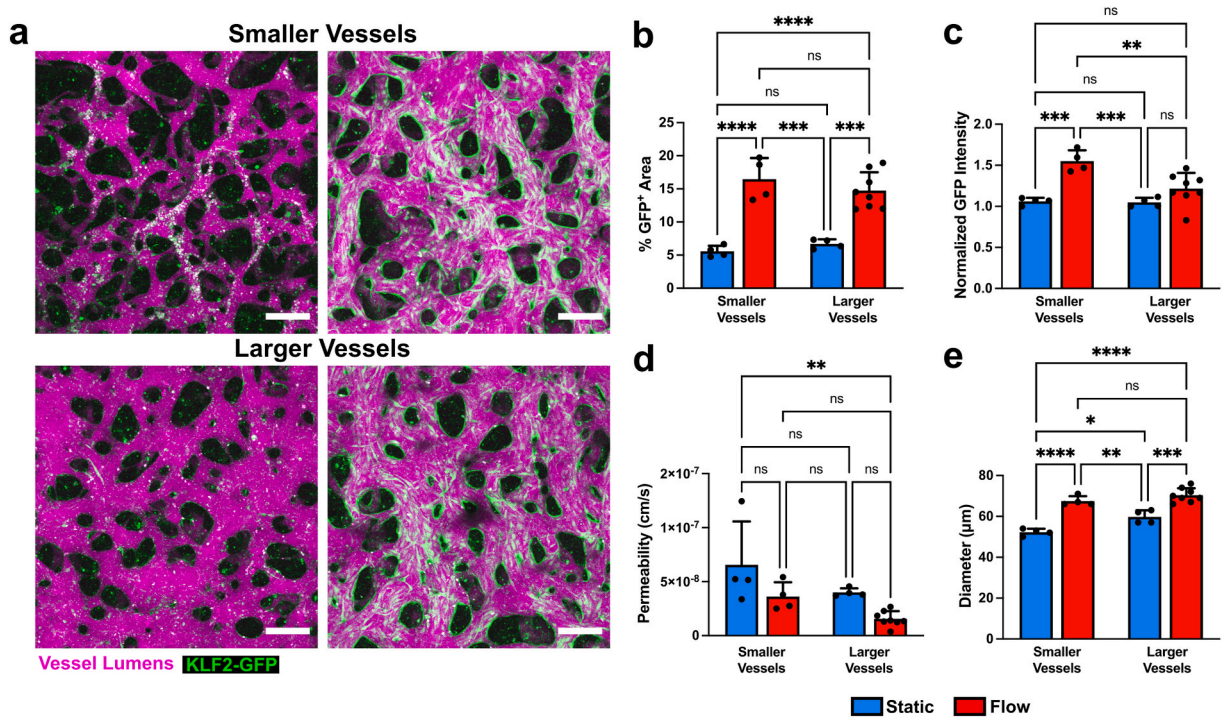

Fig. 5. Modulation of vascular responses to flow by initial vascular geometry. a MVNs with smaller (top) or larger (bottom) average diameters perfused with fluorescent dextran (magenta) under static culture and after culture under flow that activates *KLF2*-GFP expression (green). Scale bars = 200 μm. b-e Percent of total imaging area with *KLF2*-GFP signal, *KLF2*-GFP signal intensity normalized to lowest intensity static sample, vascular permeability, and average vascular diameter in smaller and larger vessels under static culture (blue) and after culture under flow (red). n = 4–8 MVNs in each group of panels b–e. * indicates $p < 0.05$, ** indicates $p < 0.01$, and **** indicates $p < 0.0001$. (For interpretation of the references to colour in this figure legend, the reader is referred to the Web version of this article.)

where *KLF2*-GFP was expressed (5.6 ± 0.8 %, n = 4 for smaller static vessels, 16.5 ± 3.2 %, n = 4 for smaller flow vessels, 6.7 ± 0.7 %, n = 4 for larger static vessels, and 14.7 ± 2.8 %, n = 8 for larger flow vessels), and the percent GFP-positive area was not significantly different between the flow groups (Fig. 5b). However, normalized GFP intensity was only significantly increased in response to flow in the MVNs with smaller vessels (1.1 ± 0.04, n = 4 for smaller static vessels, 1.5 ± 0.1, n = 4 for smaller flow vessels) and did not change significantly in response to flow in MVNs with larger vessels (1.0 ± 0.1, n = 4 for larger static vessels, 1.2 ± 0.2, n = 8 for larger flow vessels, Fig. 5c). Permeability, a measure of vascular barrier function, tended to decrease with application of flow in both smaller and larger vessels, but this effect was not statistically significant (Fig. 5d), although larger flow vessels had significantly lower permeability than static smaller vessels ($6.6 \times 10^{-8} \pm 4.0 \times 10^{-8}$ cm/s, n = 4 for smaller static vessels, $1.6 \times 10^{-8} \pm 7.0 \times 10^{-9}$ cm/s, n = 8 for larger flow vessels). Finally, vessel diameters increased in response to flow in both smaller and larger vessels (52.3 ± 1.7 μm, n = 4 for smaller static vessels, 67.5 ± 2.4 μm, n = 4 for smaller flow vessels, 59.8 ± 3.2 μm, n = 4 for larger static vessels, and 70.4 ± 3.4 μm, n = 4 for larger flow vessels, Fig. 5e). Interestingly, diameters of smaller and larger vessels under flow were not significantly different, indicating that flow can be used to achieve a similar vessel diameter endpoint, regardless of the starting vessel diameter.

Changes in vascular function in response to flow. Alongside changes in vascular geometry, we characterized the effects of flow on several functional properties of the MVNs. Cells in both MVNs cultured under either static or flow conditions display low levels of apoptosis, as indicated by immunostaining of cleaved caspase-3 (Supplementary Fig. 6). To measure vascular barrier function, we perfused MVNs with fluorescent dextran (MW = 70 kDa), acquired images of the networks and the surrounding matrix at 0 and 12 min, and measured the change in extravascular fluorescence over time (Fig. 6a). This rate of change in fluorescence, indicative of the rate of transport of dextran from the intravascular to the extra-vascular space, was used to calculate vascular permeability [6], which was significantly decreased in flow MVNs ($9.6 \times 10^{-8} \pm 6.4 \times 10^{-8}$ cm/s, n = 12 for static and $4.9 \times 10^{-8} \pm 2.0 \times 10^{-8}$ cm/s, n = 11 for flow, Fig. 6b). In addition to improving vascular barrier function, the application of flow in MVNs significantly decreased hydraulic vascular resistance across the entire MVN ($5.2 \times 10^{13} \pm 1.6 \times 10^{13}$ Pa s/m^3, n = 6 for static and $3.8 \times 10^{12} \pm 2.2 \times 10^{12}$ Pa s/m^3, n = 5 for flow, Fig. 6c). Further, we investigated the effects of flow on modulating some aspects of thrombogenicity of the vascular wall by labeling platelets with a fluorescent antibody against CD41 in suspension and perfusing them into MVNs cultured under static conditions or into MVNs cultured under flow immediately after ceasing flow and removing the devices from the pump (Fig. 6d). Fluorescent confocal imaging revealed many more platelets adhered to the MVNs under static than under flow conditions (Fig. 6e) and the percentage area covered by platelets was significantly higher in static MVNs (5.7 ± 1.8 %, n = 6 for static and 1.6 ± 0.3 %, n = 5 for flow, Fig. 6f). MVNs cultured under static conditions or under flow did not express E-selectin/P-selectin (Supplementary Fig. 7). Finally, to verify that MVNs can respond to pro-inflammatory stimuli, we treated MVNs under static and flow conditions with recombinant human IL-1β (10 units/mL) for 6 h and stained for vascular adhesion molecule-1 (VCAM-1). For MVNs cultured under flow, IL-1β was added during the last 6 h of the 48 h flow. While both static and flow untreated MVNs expressed low levels of VCAM-1, the addition of IL-1β increased VCAM-1 in both groups (Fig. 6g, Supplementary Fig. 7). Interestingly, MVNs cultured under flow also expressed E-selectin/P-selectin in response to IL-1β treatment, while static MVNs did not (Supplementary Fig. 7). Thus, MNV cultured under flow display an improved vascular barrier function, a decreased vascular network resistance, a response to pro-inflammatory stimuli and decreased platelet adhesion.

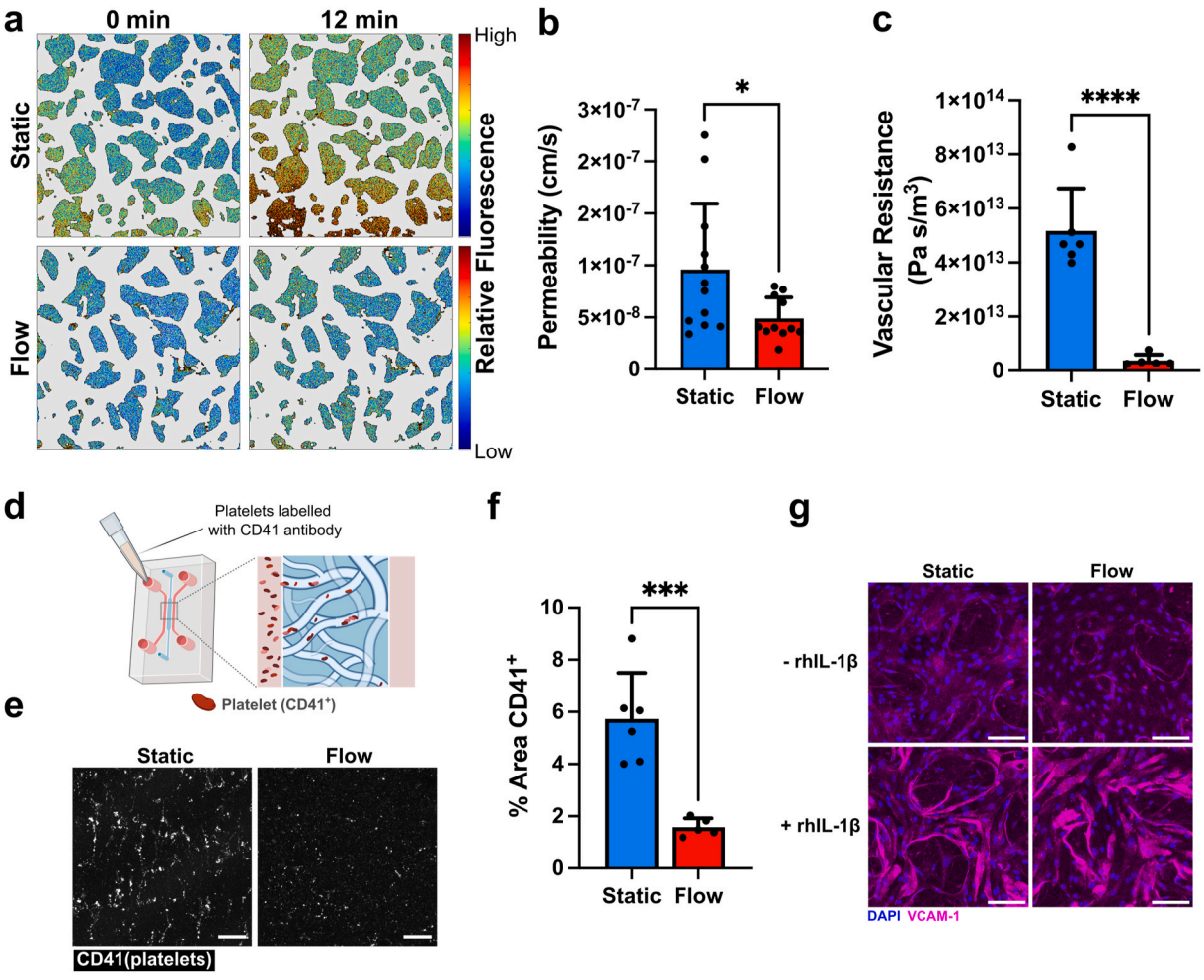

Fig. 6. Flow-induced changes in vascular function. a Heat maps of extravascular fluorescence in MVN cultured under static (top row) and flow (bottom row) conditions immediately after vascular perfusion with fluorescent dextran (left) and after 12 min (right). Scale bars = 200 μm. b Vascular permeability in MVNs cultured under static conditions or after 48 h of flow (n = 11–12 per group). c Total vascular resistance of MVNs cultured under static conditions or after 48 h of flow (n = 5–6 per group). d Schematic of experimental design for introducing platelets into MVNs. e Maximum intensity projections of CD41-labelled platelets (white) in MVNs. Networks were cultured under static conditions or exposed to flow for 68 h prior to addition of platelets in the networks. Scale bars = 200 μm. f Percent of image area covered by CD41-labelled platelets in MVN devices (n = 5–6 per group). b Representative images of VCAM-1 staining (magenta) in MVNs under static and flow conditions, with and without treatment with recombinant human IL-1β for 6 h. * indicates $p < 0.05$, *** indicates $p < 0.001$, and **** indicates $p < 0.0001$.

4. Discussion and conclusions

The regulation of EC structure and function by hemodynamic forces [30,31] makes the incorporation of flow an essential component in engineering physiologically-relevant models of the vasculature. In this study, we applied continuous, circulating flow to self-assembled MVNs in a microfluidic chip and studied the resultant changes in vascular geometry and function. Although many groups report systems with engineered vessels under flow, a majority of these constitute a single channel with a diameter over 100 μm [32–34], and sometimes with a diameter of 500 μm or more [35,36]. Our self-assembled MVNs contain vessels with an average diameter of around 50 μm, resembling the size of smaller arterioles and venules in the human body [37]. In systems similar to ours, which recapitulate a complex network of smaller-diameter vessels, flow has been achieved by applying hydrostatic pressure differences across the vascular networks [38,39], which results in decreasing fluid flow as the pressures equilibrate over time. In contrast, our device drives continuous flow through the MVNs for sustained periods of time, which is necessary for the induction of flow-related genes in the ECs.

A key feature of our system is the incorporation of a flow-sensitive EC-specific reporter, driven by the promoter of *KLF2* [21]. While many genes are regulated by shear stress [9,40], the choice of *KLF2* expression as the basis for a flow sensor is particularly attractive because, within the vasculature, the expression of this transcription factor occurs only in ECs and is induced by sustained laminar flow [19,20]. In HUVEC, *KLF2* induction is specifically tied to shear stress and is not induced by the application of cyclic strain [16], allowing us to use it as a marker of a particular type of mechanical force. Importantly, *KLF2* is a key orchestrator of endothelial gene expression programs that regulate blood vessel development, response to inflammation, thrombosis, and vascular tone [15], and therefore serves as a proxy for a well-defined endothelial phenotype. Given that differences in approach to applying flow in engineered systems can make it difficult to interpret findings across studies, reporters like the *KLF2*-GFP construct we use here can help verify whether the flow regimes applied produce a specific EC phenotype and are, therefore, comparable.

Additionally, we identified flow parameters sufficient for expression of *KLF2*-GFP in our MVNs. In agreement with previous studies [41,42], we found that two-dimensional EC monolayer preparations express *KLF2* in a majority of cells in response to 5–10 dyn/cm^2 (0.5–1 Pa) of shear stress. While the *KLF2* reporter is activated in response to shear stresses starting at 2 dyn/cm^2 (0.2 Pa) in monolayer cultures [43], it had not previously been used in three dimensional vascular preparations. We

found that applying flow for a minimum of 6 h results in robust expression of *KLF2*-GFP in MVNs, which can serve as a benchmark for other microphysiological vascular systems. After cessation of flow, the signal will decrease to 75 % of its maximum value within 12 h and will return to pre-flow levels by 24 h. The flows in our system, visualized by tracking the positions of fluorescent beads within the MVNs, appeared regular and laminar, consistent with unidirectional flows having little flow reversal that are known to activate *KLF2* [22]. Computational modeling of flow in our MVNs prior to flow-induced remodeling indicated an average wall shear stress of about 7 dyn/cm^2 (0.7 Pa), in the range of values reported for post-capillary venules [44]. At the same time, a range of wall shear stresses was present within each MVN, reflecting the heterogeneity of branch geometry and size within each device.

MVNs exposed to GFP-inducing flows exhibited a marked increase in diameter. It has long been known that blood flow can regulate vascular diameter [45] and outward remodeling has been associated with high shear stresses [46]. In the developing murine vasculature, hemodynamic forces from blood flow are necessary for vascular remodeling [47] and cause increases in vascular diameter by inducing vessel fusion in regions of high flow and EC migration towards regions with greater flow, rather than EC proliferation [48]. This type of vascular remodeling occurs when EC experience shear stresses outside of a physiological set point [14] and results in changes in diameter that ultimately restore shear stress levels to optimal, vasculature-stabilizing levels [31].

We found that flow conditioning did not increase the range of vessel diameters in the MVN system, but caused a rightward shift in the distribution of vessel diameters and resulted in longer and less-branched vessels throughout the MVNs. The presence of fewer but larger vessels along with the establishment of preferential flow paths as media was circulated through the MVNs, evident in our computational simulations of flow, suggests the occurrence of vascular pruning. This is a likely explanation for the widespread expression of *KLF2*-GFP in virtually all vessels after 48 h of flow, since vessels along preferential paths were exposed to flow and activated the flow-responsive gene while other vessels were subjected to infrequent or low flow and regressed. Remodeling of vascular geometry in response to flow has been described *in vivo*, in multiple organisms. Chen et al. described hemodynamic regulation of vascular pruning during development of the zebrafish midbrain, where pruning was initiated in vascular segments with low and variable blood flow [49]. ECs from these pruning segments migrated to adjacent unpruned segments with higher flow, resulting in overall simplification of complex vascular networks over time [49]. Observations in the developing mouse retina have also revealed shear stress-mediated cellular polarization that directs migration toward high flow branches, resulting in destabilization and eventual regression of low-flow branches, with net movement toward and stabilization of high-flow branches [50].

Cellular elongation and alignment along the direction of flow is often observed in planar EC preparations exposed to laminar shear stresses [51,52]. In our MVNs, ECs were highly elongated and oriented along the long axis of each vascular branch, even in static culture. This high degree of elongation and orientation was maintained with flow. Having established vascular remodeling and EC enlargement in our system over the course of 48 h of flow, future work can focus on observing individual ECs within MVNs over time to determine the mechanisms of vessel widening and pruning.

In addition to structural changes, we observed numerous functional changes in MVNs cultured under flow. MVNs under flow had a significantly lower vascular resistance than those cultured under static conditions, in keeping with their overall larger vessel diameter. We also assessed vascular barrier function by perfusing fluorescent dextran through the MVNs and measuring changes in fluorescent intensity in the vascular and extravascular compartments [6] over time. MVNs under flow had a significantly decreased permeability, indicating a tighter endothelial barrier. This improvement in barrier function in response to flow is in line with previous studies. In straight channel vessels formed within collagen gels, flow improved vascular barrier function and extended the lifespan of vessels. In this system, improvements in barrier function and more organized and uniform expression of VE-cadherin at EC junctions were attributed to increased shear stresses and were not altered by changes in transmural pressure [53]. In our studies, application of flow to improve the barrier function increases the physiological relevance of engineered MVNs. While it has been shown that three-dimensional MVN preparations have lower permeabilities than monolayer cultures, the further improvement in barrier function through the application of flow makes them similar to *in vivo* models for barrier studies [6].

Haase and colleagues also applied circulating flow for 48 h to complex MVNs [39]. While they reported that continuous flow staves off decreases in vascular diameter observed in static cultures over time, and causes a slight, but non-significant, improvement in vascular barrier function, our findings are more prominent: application of circulating flow in our system produced significant increases vascular in diameter and improved barrier function.

Finally, we assessed the anti-thrombogenic effect of *KLF2* reporter-inducing flow in our MVNs. Our system was able to recapitulate this important aspect of flow, as MVNs cultured under flow exhibited adhesion of significantly fewer platelets than MVNs cultured under static conditions. It has been previously demonstrated that preconditioning EC monolayers with *KLF2*-activating flow decreasedIL-1β-dependent adhesion of leukocytes [15] and our three-dimensional MVNs also confirm the anti-thrombogenic feature of flow-conditioning and respond to IL-1β activation by expressing VCAM-1.

The *KLF2*-GFP EC sensor deployed in our system is a particularly useful tool because it serves as a visual indicator of successful perfusion through the MVNs. We took advantage of this readout to characterize the effects of flow on MVNs with different starting geometries. We started with smaller or larger vessels, applied flow using identical pump settings, and evaluated MVNs expressing *KLF2*-GFP after 48 h. While flow increased average vascular diameter of MVNs with both smaller and larger initial vessels, the diameters of MVNs after application of flow were indistinguishable, regardless of the initial diameters. Since the geometry of self-assembled engineered networks like these depends on multiple factors and conditions, (including cell counts, thrombin concentrations, fibrinogen efficacy, and time of gel injection into the device), which are prone to human and reagent variability, flow can serve as a means of reducing variability in samples across batches and users. While permeability tended to decrease with flow in both smaller and larger MVNs, it was striking that the lowest permeability was observed in the larger vessels group exposed to flow. While we evaluated permeability after 48 h of flow, we did not characterize changes at earlier timepoints, and it is possible that a period of increased permeability would be observed after initiation of flow, when the cells are undergoing junctional rearrangement [54]. In this case, MVNs that started out with smaller vessels would have to undergo more drastic structural changes to reach the 48-h endpoint we observed and might reach their minimum permeability later than MVNs that started out with larger vessels and require far less structural adaptation.

The system that we have presented here, which incorporates MVNs with a *KLF2*-GFP reporter and a microfluidic pump, can be modified and expanded for future studies aimed at understanding the effects of flow on endothelial cell biology. For instance, MVNs could be formed from human pluripotent stem cell-derived EC [7] to study how shear stresses impact their phenotype and arteriovenous specification [55,56]. Further, alternative flow profiles could be explored using the *KLF2*-GFP readout, since it has been found that while *KLF2* expression in response to high shear stress levels can be further increased by applying pulsatile flows [16].

Funding

This work was supported by the National Institutes of Health [grant numbers R21HL152367, T32HL007627, and T32EB016652].

CRediT authorship contribution statement

Adriana Blazeski: Writing – review & editing, Writing – original draft, Visualization, Software, Methodology, Investigation, Formal analysis, Conceptualization. **Marie A. Floryan:** Writing – review & editing, Resources. **Yuzhi Zhang:** Investigation. **Oscar R. Fajardo Ramírez:** Resources. **Elamaran Meibalan:** Investigation. **Jesús Ortiz-Urbina:** Writing – review & editing, Investigation. **Emmanouil Angelidakis:** Writing – review & editing, Methodology, Investigation. **Sarah E. Shelton:** Writing – review & editing, Methodology, Investigation. **Roger D. Kamm:** Writing – review & editing, Supervision, Funding acquisition, Conceptualization. **Guillermo García-Cardeña:** Writing – review & editing, Supervision, Funding acquisition, Conceptualization.

Declaration of competing interest

The authors declare that they have no known competing financial interests or personal relationships that could have appeared to influence the work reported in this paper.

Data availability

Data will be made available on request.

Appendix A. Supplementary data

Supplementary data to this article can be found online at https://doi.org/10.1016/j.biomaterials.2024.122686.

References

[1] M.L. Ewald, Y.-H. Chen, A.P. Lee, C.C.W. Hughes, The vascular niche in next generation microphysiological systems, Lab Chip 21 (2021) 3244–3262, https://doi.org/10.1039/d1lc00530h.
[2] J.A. Whisler, M.B. Chen, R.D. Kamm, Control of perfusable microvascular network morphology using a multiculture microfluidic system, Tissue Eng. C Methods 20 (2014) 543–552, https://doi.org/10.1089/ten.TEC.2013.0370.
[3] S. Kim, H. Lee, M. Chung, N.L. Jeon, Engineering of functional, perfusable 3D microvascular networks on a chip, Lab Chip 13 (2013) 1489–1500, https://doi.org/10.1039/c3lc41320a.
[4] M.L. Moya, Y.-H. Hsu, A.P. Lee, C.C.W. Hughes, S.C. George, *In vitro* perfused human capillary networks, Tissue Eng. C Methods 19 (2013) 730–737, https://doi.org/10.1089/ten.TEC.2012.0430.
[5] S. Zhang, Z. Wan, G. Pavlou, A.X. Zhong, L. Xu, R.D. Kamm, Interstitial flow promotes the formation of functional microvascular networks *in vitro* through upregulation of matrix metalloproteinase-2, Adv. Funct. Mater. 32 (2022) 2206767, https://doi.org/10.1002/adfm.202206767.
[6] G.S. Offeddu, K. Haase, M.R. Gillrie, R. Li, O. Morozova, D. Hickman, C.G. Knutson, R.D. Kamm, An on-chip model of protein paracellular and transcellular permeability in the microcirculation, Biomaterials 212 (2019) 115–125, https://doi.org/10.1016/j.biomaterials.2019.05.022.
[7] M. Campisi, Y. Shin, T. Osaki, C. Hajal, V. Chiono, R.D. Kamm, 3D self-organized microvascular model of the human blood-brain barrier with endothelial cells, pericytes and astrocytes, Biomaterials 180 (2018) 117–129, https://doi.org/10.1016/j.biomaterials.2018.07.014.
[8] S. Kim, Z. Wan, J.S. Jeon, R.D. Kamm, Microfluidic vascular models of tumor cell extravasation, Front. Oncol. 12 (2022), https://doi.org/10.3389/fonc.2022.1052192.
[9] G. Garcia-Cardeña, J. Comander, K.R. Anderson, B.R. Blackman, M.A. Gimbrone, Biomechanical activation of vascular endothelium as a determinant of its functional phenotype, Proc. Natl. Acad. Sci. U.S.A. 98 (2001) 4478–4485, https://doi.org/10.1073/pnas.071052598.
[10] P.F. Davies, Flow-mediated endothelial mechanotransduction, Physiol. Rev. 75 (1995) 519–560, https://doi.org/10.1152/physrev.1995.75.3.519.
[11] C.A. Dessalles, C. Leclech, A. Castagnino, A.I. Barakat, Integration of substrate- and flow-derived stresses in endothelial cell mechanobiology, Commun. Biol. 4 (2021) 764, https://doi.org/10.1038/s42003-021-02285-w.
[12] P. Campinho, A. Vilfan, J. Vermot, Blood flow forces in shaping the vascular system: a focus on endothelial cell behavior, Front. Physiol. 11 (2020) 552, https://doi.org/10.3389/fphys.2020.00552.
[13] A.M. Malek, S.L. Alper, S. Izumo, Hemodynamic shear stress and its role in atherosclerosis, JAMA 282 (1999) 2035–2042, https://doi.org/10.1001/jama.282.21.2035.
[14] N. Baeyens, S. Nicoli, B.G. Coon, T.D. Ross, K. Van den Dries, J. Han, H. M. Lauridsen, C.O. Mejean, A. Eichmann, J.-L. Thomas, J.D. Humphrey, M. A. Schwartz, Vascular remodeling is governed by a VEGFR3-dependent fluid shear stress set point, Elife 4 (2015), https://doi.org/10.7554/eLife.04645.
[15] K.M. Parmar, H.B. Larman, G. Dai, Y. Zhang, E.T. Wang, S.N. Moorthy, J.R. Kratz, Z. Lin, M.K. Jain, M.A. Gimbrone, G. García-Cardeña, Integration of flow-dependent endothelial phenotypes by Kruppel-like factor 2, J. Clin. Invest. 116 (2006) 49–58, https://doi.org/10.1172/JCI24787.
[16] R.J. Dekker, J. V van Thienen, J. Rohlena, S.C. de Jager, Y.W. Elderkamp, J. Seppen, C.J.M. de Vries, E.A.L. Biessen, T.J.C. van Berkel, H. Pannekoek, A.J. G. Horrevoets, Endothelial KLF2 links local arterial shear stress levels to the expression of vascular tone-regulating genes, Am. J. Pathol. 167 (2005) 609–618, https://doi.org/10.1016/S0002-9440(10)63002-7.
[17] P. Sangwung, G. Zhou, L. Nayak, E.R. Chan, S. Kumar, D.-W. Kang, R. Zhang, X. Liao, Y. Lu, K. Sugi, H. Fujioka, H. Shi, S.D. Lapping, C.C. Ghosh, S.J. Higgins, S. M. Parikh, H. Jo, M.K. Jain, KLF2 and KLF4 control endothelial identity and vascular integrity, JCI Insight 2 (2017), https://doi.org/10.1172/jci.insight.91700.
[18] G.B. Atkins, Y. Wang, G.H. Mahabeleshwar, H. Shi, H. Gao, D. Kawanami, V. Natesan, Z. Lin, D.I. Simon, M.K. Jain, Hemizygous deficiency of Krüppel-like factor 2 augments experimental atherosclerosis, Circ. Res. 103 (2008) 690–693, https://doi.org/10.1161/CIRCRESAHA.108.184663.
[19] R.J. Dekker, S. van Soest, R.D. Fontijn, S. Salamanca, P.G. de Groot, E. VanBavel, H. Pannekoek, A.J.G. Horrevoets, Prolonged fluid shear stress induces a distinct set of endothelial cell genes, most specifically lung Krüppel-like factor (KLF2), Blood 100 (2002) 1689–1698, https://doi.org/10.1182/blood-2002-01-0046.
[20] S. SenBanerjee, Z. Lin, G.B. Atkins, D.M. Greif, R.M. Rao, A. Kumar, M.W. Feinberg, Z. Chen, D.I. Simon, F.W. Luscinskas, T.M. Michel, M.A. Gimbrone, G. García-Cardeña, M.K. Jain, KLF2 Is a novel transcriptional regulator of endothelial proinflammatory activation, J. Exp. Med. 199 (2004) 1305–1315, https://doi.org/10.1084/jem.20031132.
[21] B.R. Slegtenhorst, O.R. Fajardo Ramirez, Y. Zhang, Z. Dhanerawala, S.G. Tullius, G. García-Cardeña, A mechano-activated cell reporter system as a proxy for flow-dependent endothelial atheroprotection, SLAS Discov. 23 (2018) 869–876, https://doi.org/10.1177/2472555218761101.
[22] G. Dai, M.R. Kaazempur-Mofrad, S. Natarajan, Y. Zhang, S. Vaughn, B. R. Blackman, R.D. Kamm, G. García-Cardeña, M.A. Gimbrone, Distinct endothelial phenotypes evoked by arterial waveforms derived from atherosclerosis-susceptible and -resistant regions of human vasculature, Proc. Natl. Acad. Sci. U.S.A. 101 (2004) 14871–14876, https://doi.org/10.1073/pnas.0406073101.
[23] M.B. Chen, J.A. Whisler, J. Fröse, C. Yu, Y. Shin, R.D. Kamm, On-chip human microvasculature assay for visualization and quantification of tumor cell extravasation dynamics, Nat. Protoc. 12 (2017) 865–880, https://doi.org/10.1038/nprot.2017.018.
[24] C. Hajal, G.S. Offeddu, Y. Shin, S. Zhang, O. Morozova, D. Hickman, C.G. Knutson, R.D. Kamm, Engineered human blood-brain barrier microfluidic model for vascular permeability analyses, Nat. Protoc. 17 (2022) 95–128, https://doi.org/10.1038/s41596-021-00635-w.
[25] G.S. Offeddu, J.C. Serrano, S.W. Chen, S.E. Shelton, Y. Shin, M. Floryan, R. D. Kamm, Microheart: a microfluidic pump for functional vascular culture in microphysiological systems, J. Biomech. 119 (2021) 110330, https://doi.org/10.1016/j.jbiomech.2021.110330.
[26] A. Rota, L. Possenti, G.S. Offeddu, M. Senesi, A. Stucchi, I. Venturelli, T. Rancati, P. Zunino, R.D. Kamm, M.L. Costantino, A three-dimensional method for morphological analysis and flow velocity estimation in microvasculature on-a-chip, Bioeng. Transl. Med. 8 (2023) e10557, https://doi.org/10.1002/btm2.10557.
[27] J.A. Montoya-Zegarra, E. Russo, P. Runge, M. Jadhav, A.-H. Willrodt, S. Stoma, S. F. Nørrelykke, M. Detmar, C. Halin, AutoTube: a novel software for the automated morphometric analysis of vascular networks in tissues, Angiogenesis 22 (2019) 223–236, https://doi.org/10.1007/s10456-018-9652-3.
[28] E. Angelidakis, S. Chen, S. Zhang, Z. Wan, R.D. Kamm, S.E. Shelton, Impact of fibrinogen, fibrin thrombi, and thrombin on cancer cell extravasation using *in vitro* microvascular networks, Adv. Healthcare Mater. 12 (2023) e2202984, https://doi.org/10.1002/adhm.202202984.
[29] G.S. Offeddu, L. Possenti, J.T. Loessberg-Zahl, P. Zunino, J. Roberts, X. Han, D. Hickman, C.G. Knutson, R.D. Kamm, Application of transmural flow across *in vitro* microvasculature enables direct sampling of interstitial therapeutic molecule distribution, Small 15 (2019) e1902393, https://doi.org/10.1002/smll.201902393.
[30] M.A. Gimbrone, G. García-Cardeña, Endothelial cell dysfunction and the pathobiology of atherosclerosis, Circ. Res. 118 (2016) 620–636, https://doi.org/10.1161/CIRCRESAHA.115.306301.
[31] N. Baeyens, C. Bandyopadhyay, B.G. Coon, S. Yun, M.A. Schwartz, Endothelial fluid shear stress sensing in vascular health and disease, J. Clin. Invest. 126 (2016) 821–828, https://doi.org/10.1172/JCI83083.
[32] C.A. Dessalles, C. Ramón-Lozano, A. Babataheri, A.I. Barakat, Luminal flow actuation generates coupled shear and strain in a microvessel-on-chip, Biofabrication 14 (2021), https://doi.org/10.1088/1758-5090/ac2baa.
[33] J.J. Tronolone, J. Lam, A. Agrawal, K. Sung, Pumpless, modular, microphysiological systems enabling tunable perfusion for long-term cultivation of

endothelialized lumens, Biomed. Microdevices 23 (2021) 25, https://doi.org/10.1007/s10544-021-00562-3.
[34] C. Poussin, B. Kramer, H.L. Lanz, A. Van den Heuvel, A. Laurent, T. Olivier, M. Vermeer, D. Peric, K. Baumer, R. Dulize, E. Guedj, N. V Ivanov, M.C. Peitsch, J. Hoeng, J. Joore, 3D human microvessel-on-a-chip model for studying monocyte-to-endothelium adhesion under flow - application in systems toxicology, ALTEX 37 (2020) 47–63, https://doi.org/10.14573/altex.1811301.
[35] C.F. Buchanan, S.S. Verbridge, P.P. Vlachos, M.N. Rylander, Flow shear stress regulates endothelial barrier function and expression of angiogenic factors in a 3D microfluidic tumor vascular model, Cell Adhes. Migrat. 8 (2014) 517–524, https://doi.org/10.4161/19336918.2014.970001.
[36] C.G.M. van Dijk, M.M. Brandt, N. Poulis, J. Anten, M. van der Moolen, L. Kramer, E.F.G.A. Homburg, L. Louzao-Martinez, J. Pei, M.M. Krebber, B.W.M. van Balkom, P. de Graaf, D.J. Duncker, M.C. Verhaar, R. Luttge, C. Cheng, A new microfluidic model that allows monitoring of complex vascular structures and cell interactions in a 3D biological matrix, Lab Chip 20 (2020) 1827–1844, https://doi.org/10.1039/d0lc00059k.
[37] M. Thiriet, K.H. Parker, Physiology and pathology of the cardiovascular system: a physical perspective, in: Cardiovascular Mathematics, Springer, Milan, Milano, 2009, pp. 1–45, https://doi.org/10.1007/978-88-470-1152-6_1.
[38] H. Sano, M. Watanabe, T. Yamashita, K. Tanishita, R. Sudo, Control of vessel diameters mediated by flow-induced outward vascular remodeling *in vitro*, Biofabrication 12 (2020) 045008, https://doi.org/10.1088/1758-5090/ab9316.
[39] K. Haase, F. Piatti, M. Marcano, Y. Shin, R. Visone, A. Redaelli, M. Rasponi, R. D. Kamm, Physiologic flow-conditioning limits vascular dysfunction in engineered human capillaries, Biomaterials 280 (2022) 121248, https://doi.org/10.1016/j.biomaterials.2021.121248.
[40] J.N. Topper, J. Cai, D. Falb, M.A. Gimbrone, Identification of vascular endothelial genes differentially responsive to fluid mechanical stimuli: cyclooxygenase-2, manganese superoxide dismutase, and endothelial cell nitric oxide synthase are selectively up-regulated by steady laminar shear stress, Proc. Natl. Acad. Sci. U.S.A. 93 (1996) 10417–10422, https://doi.org/10.1073/pnas.93.19.10417.
[41] A. Doddaballapur, K.M. Michalik, Y. Manavski, T. Lucas, R.H. Houtkooper, X. You, W. Chen, A.M. Zeiher, M. Potente, S. Dimmeler, R.A. Boon, Laminar shear stress inhibits endothelial cell metabolism via KLF2-mediated repression of PFKFB3, Arterioscler. Thromb. Vasc. Biol. 35 (2015) 137–145, https://doi.org/10.1161/ATVBAHA.114.304277.
[42] B.G. Coon, S. Timalsina, M. Astone, Z.W. Zhuang, J. Fang, J. Han, J. Themen, M. Chung, Y.J. Yang-Klingler, M. Jain, K.K. Hirschi, A. Yamamato, L.-E. Trudeau, M. Santoro, M.A. Schwartz, A mitochondrial contribution to anti-inflammatory shear stress signaling in vascular endothelial cells, J. Cell Biol. 221 (2022), https://doi.org/10.1083/jcb.202109144.
[43] R.J. Luu, B.C. Hoefler, A.L. Gard, C.R. Ritenour, M.T. Rogers, E.S. Kim, J. R. Coppeta, B.P. Cain, B.C. Isenberg, H. Azizgolshani, O.R. Fajardo-Ramirez, G. García-Cardeña, M.P. Lech, L. Tomlinson, J.L. Charest, C. Williams, Fibroblast activation in response to TGFβ1 is modulated by co-culture with endothelial cells in a vascular organ-on-chip platform, Front. Mol. Biosci. 10 (2023) 1160851, https://doi.org/10.3389/fmolb.2023.1160851.
[44] A.G. Koutsiaris, S. V Tachmitzi, N. Batis, M.G. Kotoula, C.H. Karabatsas, E. Tsironi, D.Z. Chatzoulis, Volume flow and wall shear stress quantification in the human conjunctival capillaries and post-capillary venules *in vivo*, Biorheology 44 (2007) 375–386. http://www.ncbi.nlm.nih.gov/pubmed/18401076.
[45] J.L. Tuttle, R.D. Nachreiner, A.S. Bhuller, K.W. Condict, B.A. Connors, B.P. Herring, M.C. Dalsing, J.L. Unthank, Shear level influences resistance artery remodeling: wall dimensions, cell density, and eNOS expression, Am. J. Physiol.-Heart. Circ. Physiol. 281 (2001) H1380–H1389. https://doi.org/10.1152/ajpheart.2001.281.3.H1380.
[46] F. Tronc, M. Wassef, B. Esposito, D. Henrion, S. Glagov, A. Tedgui, Role of NO in flow-induced remodeling of the rabbit common carotid artery, Arterioscler. Thromb. Vasc. Biol. 16 (1996) 1256–1262, https://doi.org/10.1161/01.ATV.16.10.1256.
[47] J.L. Lucitti, E.A. V Jones, C. Huang, J. Chen, S.E. Fraser, M.E. Dickinson, Vascular remodeling of the mouse yolk sac requires hemodynamic force, Development 134 (2007) 3317–3326, https://doi.org/10.1242/dev.02883.
[48] R.S. Udan, T.J. Vadakkan, M.E. Dickinson, Dynamic responses of endothelial cells to changes in blood flow during vascular remodeling of the mouse yolk sac, Development 140 (2013) 4041–4050, https://doi.org/10.1242/dev.096255.
[49] Q. Chen, L. Jiang, C. Li, D. Hu, J. Bu, D. Cai, J. Du, Haemodynamics-driven developmental pruning of brain vasculature in zebrafish, PLoS Biol. 10 (2012) e1001374, https://doi.org/10.1371/journal.pbio.1001374.
[50] C.A. Franco, M.L. Jones, M.O. Bernabeu, I. Geudens, T. Mathivet, A. Rosa, F. M. Lopes, A.P. Lima, A. Ragab, R.T. Collins, L.-K. Phng, P. V Coveney, H. Gerhardt, Dynamic endothelial cell rearrangements drive developmental vessel regression, PLoS Biol. 13 (2015) e1002125, https://doi.org/10.1371/journal.pbio.1002125.
[51] H. Avari, K.A. Rogers, E. Savory, Quantification of morphological modulation, F-actin remodeling, and PECAM-1 (CD-31) redistribution in endothelial cells in response to fluid-induced shear stress under various flow conditions, J. Biomech. Eng. 141 (2019), https://doi.org/10.1115/1.4042601.
[52] C. Wang, B.M. Baker, C.S. Chen, M.A. Schwartz, Endothelial cell sensing of flow direction, Arterioscler. Thromb. Vasc. Biol. 33 (2013) 2130–2136, https://doi.org/10.1161/ATVBAHA.113.301826.
[53] G.M. Price, K.H.K. Wong, J.G. Truslow, A.D. Leung, C. Acharya, J. Tien, Effect of mechanical factors on the function of engineered human blood microvessels in microfluidic collagen gels, Biomaterials 31 (2010) 6182–6189, https://doi.org/10.1016/j.biomaterials.2010.04.041.
[54] H. Jo, R.O. Dull, T.M. Hollis, J.M. Tarbell, Endothelial albumin permeability is shear dependent, time dependent, and reversible, Am. J. Physiol. 260 (1991) H1992–H1996, https://doi.org/10.1152/ajpheart.1991.260.6.H1992.
[55] S. Arora, A.J.Y. Lam, C. Cheung, E.K.F. Yim, Y.-C. Toh, Determination of critical shear stress for maturation of human pluripotent stem cell-derived endothelial cells towards an arterial subtype, Biotechnol. Bioeng. 116 (2019) 1164–1175, https://doi.org/10.1002/bit.26910.
[56] E. Helle, M. Ampuja, L. Antola, R. Kivelä, Flow-induced transcriptomic remodeling of endothelial cells derived from human induced pluripotent stem cells, Front. Physiol. 11 (2020) 591450, https://doi.org/10.3389/fphys.2020.591450.